

Hadamard Random Forest: Reconstructing real-valued quantum states with exponential reduction in measurement settings

Zhixin Song,^{1,*} Hang Ren,² Melody Lee,³ Bryan Gard,⁴
Nicolas Renaud,^{5,6} and Spencer H. Bryngelson^{3,7,8}

¹*School of Physics, Georgia Institute of Technology, Atlanta, GA, USA*

²*Berkeley Center for Quantum Information and Computation, Berkeley, CA, USA*

³*School of Computational Science & Engineering,
Georgia Institute of Technology, Atlanta, GA, USA*

⁴*CIPHER, Georgia Tech Research Institute, Atlanta, GA, USA*

⁵*Netherlands eScience Center, Matrix Building III, Amsterdam, The Netherlands*

⁶*Quantum Application Lab, Science Park,
Startup Village, Amsterdam, The Netherlands*

⁷*Daniel Guggenheim School of Aerospace Engineering,
Georgia Institute of Technology, Atlanta, GA, USA*

⁸*George W. Woodruff School of Mechanical Engineering,
Georgia Institute of Technology, Atlanta, GA, USA*

Abstract

Quantum tomography is a crucial tool for characterizing quantum states and devices and estimating nonlinear properties of the systems. Performing full quantum state tomography on an N_q qubit system requires an exponentially increasing overhead with $\mathcal{O}(3^{N_q})$ distinct Pauli measurement settings to resolve all complex phases and reconstruct the density matrix. However, many potential quantum computing applications, such as linear system solves, require only real-valued amplitudes. We introduce a readout method for real-valued quantum states that reduces measurement settings required for state vector reconstruction to $\mathcal{O}(N_q)$; the post-processing cost remains exponential $\Omega(2^{N_q})$. This approach offers a substantial speedup over conventional tomography. We experimentally validate our method up to 10 qubits on the latest available IBM quantum processor and demonstrate that it accurately extracts key properties such as entanglement and magic. Our method also outperforms the standard SWAP test for state overlap estimation. This calculation resembles a numerical integration in certain cases and can be applied to extract nonlinear properties, which are important in application fields. We further implement the method to readout the solution from a quantum linear solver.

1 Introduction

Efficient linear system solvers play a vital role in modern scientific computing and engineering challenges, from accelerating the training of large-scale machine learning models [1] to sophisticated fluid dynamics simulations [2]. Quantum approaches to linear system solves have garnered attention due to their potential to outperform classical methods [3, 4]. In particular, state-of-the-art quantum

* zsong300@gatech.edu

linear system algorithms (QLSA) [5–8] promise super-polynomial speedups in the fault-tolerant regime, where resource-intensive quantum error correction protocols and data encoding schemes such as block-encoding are required. Despite these advances, the quantum readout problem [9] may still limit the performance of many claims of potential quantum advantage. When studying quantum many-body systems, desired state properties can be extracted efficiently, including magnetization, correlation functions, and entanglement entropy [10]. However, in many other scientific problems where QLSA is favorable, the desired properties are nonlinear and involve non-Hermitian observables, making it challenging to construct a measurement scheme even using the powerful classical shadow tomography [11]. The typical approach is to reconstruct the state through tomographic methods or amplitude estimation [12, 13] and then apply post-processing to extract the relevant properties [14, 15].

Efficient quantum state reconstruction is a central task in quantum information science, enabling characterization of quantum states and modeling of quantum devices [16–18]. The standard full quantum state tomography (FQST) method [19] requires an exponential number of measurement settings to iterate over the Pauli basis $\{\sigma_x, \sigma_y, \sigma_z\}$ in each qubit. Moreover, the post-processing typically relies on resource-intensive maximum likelihood estimation (MLE) to ensure the reconstructed state $\tilde{\rho}$ is physical [20].

Approaches have been developed to address the challenges in FQST. Some methods reduce measurement costs by exploiting the low-rank structure of density matrices using compressed sensing [21] or by leveraging limited entanglement structures [22]. More recent techniques combine parallel measurements to further decrease required resources, as seen in quantum overlapping tomography [23, 24], with tensor network learning approaches [25–27]. However, these methods rely on assumptions about the quantum state’s structure or involve additional learning processes with unclear post-processing scaling.

We show that for QLSA solves involving only real-valued states, reconstructing such states requires a linear number of measurement settings instead of an exponential overhead. Real-valued states arise naturally in many other quantum algorithms, including Grover’s search [28] and the Bernstein–Vazirani algorithm [29]. With carefully injected resource states, one can achieve universal computation with real-valued states [30].

Similar ideas have been explored for real-valued observables in classical shadow tomography [31]. This work introduces the *Hadamard Random Forest* (HRF), a technique for reconstructing real-valued quantum states. By restricting the relative phase from a complex number to $\{\pm 1\}$, HRF resolves the phases exclusively in the σ_x basis combined with a specialized random forest algorithm [32]. We validate HRF on IBM’s quantum hardware for up to 10 qubits and compare its performance against FQST for up to 5 qubits. In these experiments, HRF outperforms FQST in reconstruction accuracy and runtime. HRF accurately estimates state properties from near-term hardware sampling results, including quantum entanglement, magic, and state overlap. We implement the method to a variational quantum linear system solve [33]. These results support the practical hardware application of HRF.

2 Methods

2.1 Reconstructing quantum states

Given an N_q qubit density matrix ρ , it can be expanded as,

$$\rho = \frac{1}{2^{N_q}} \sum_{i,j,\dots,\ell=0}^3 c_{ij\dots\ell} \underbrace{\sigma_i^{(1)} \otimes \sigma_j^{(2)} \dots \otimes \sigma_\ell^{(N_q)}}_{N_q \text{ qubit global observable}}, \quad (1)$$

where $c_{ij\dots\ell} \in \mathbb{C}$ and each $\sigma_0 = I, \sigma_{1,2,3} = \sigma_{x,y,z}$. After collecting 3^{N_q} global measurement statistics (each contains 2^{N_q} outcomes), the post-processing involves a maximum likelihood estimation (MLE) to ensure the reconstructed state $\tilde{\rho}$ is physical, i.e. positive semi-definite $\tilde{\rho} \geq 0$ with unit trace $\text{Tr}(\tilde{\rho}) = 1$ as illustrated in [fig. 1](#).

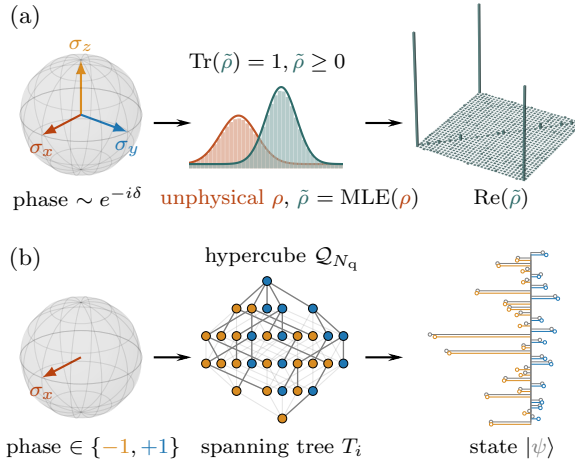


FIG. 1: Comparison between FQST (a) and the present HRF method (b) for an $N_q = 5$ case. FQST requires measuring each qubit in the Pauli basis, resulting in $3^5 = 243$ measurement settings. HRF only requires 6.

Consider an N_q qubit real-valued state

$$|\psi\rangle = U_{\text{prep.}} |0\rangle^{\otimes N_q} = \sum_{j=0}^{2^{N_q}-1} \psi_j |j\rangle, \quad (2)$$

where $U_{\text{prep.}}$ is the unitary corresponding to the state preparation circuit and $\psi_j = \text{sgn}(\psi_j) \cdot |\psi_j| \in \mathbb{R}$. The basis states $|j\rangle$ are ordered according to the lexicographical order of their bit-string representations. HRF reconstructs the corresponding state vector by sampling $N_q + 1$ circuits. The first circuit measures in the standard computational σ_z basis, evaluating the amplitudes $|\psi_j|$ by sampling the probability distribution $\{|\psi_j|^2\}$. Then, one measures each qubit in the σ_x basis, resulting in an additional N_q circuits to sample, which can be achieved by adding a Hadamard gate to rotate the measurement basis for qubit ordering and circuit construction (see supplementary information). Applying a Hadamard gate on the $(N_q - k - 1)$ -th qubit and sampling the output

leads to the new amplitude vector $|\psi^k\rangle$, where ψ_j^k and $\psi_{j+2^k}^k$ contain the superposition of original amplitudes as

$$\psi_{j,j+2^k}^k = \frac{1}{\sqrt{2}} (\psi_j \pm \psi_{j+2^k}). \quad (3)$$

This computation leads to $(N_q + 1) \times (2^{N_q})$ total probabilities. One determines the relative signs between two amplitudes $s_{j,j+2^k} := \text{sgn}(\psi_j \psi_{j+2^k})$ by querying the sampling results $\{|\psi_j^k|^2\}_{k=0}^{N_q-1}$ as

$$s_{j,j+2^k} = \text{sgn} \left[\underbrace{2|\psi_j^k|^2}_{\text{new prob.}} - \underbrace{|\psi_j|^2 - |\psi_{j+2^k}|^2}_{\text{original prob.}} \right]. \quad (4)$$

All 2^{N_q} signs ($s_j := \text{sgn}(\psi_j)$) follow by tracing the path from the root amplitude ψ_0 (assuming $\psi_0 > 0$) to the nodes ψ_j and repeatedly applying the sign determination procedure of (4). Identifying such paths is equivalent to finding spanning trees T_i on the hypercube graph \mathcal{Q}_{N_q} with 2^{N_q} nodes and $N_q 2^{(N_q-1)}$ edges. The edge exists only when the node index differs by a power of 2. For example, \mathcal{Q}_5 contains 80 edges (light gray) as illustrated in fig. 2 (a).

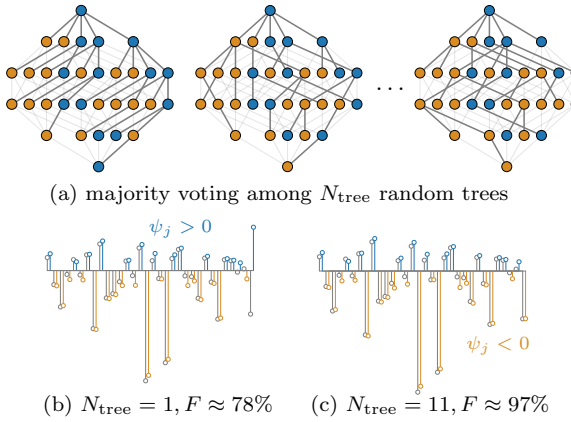


FIG. 2: Demonstration of using multiple spanning trees T_i to form a random forest and deploy a majority voting scheme to determine the signs. (a) Spanning trees in \mathcal{Q}_5 . The dark blue color is $\text{sgn}(\psi_j) = +1$ and light orange is $\text{sgn}(\psi_j) = -1$. (b) the last three signs are incorrectly determined for a single tree. (c) No sign error when using 11 trees.

\mathcal{Q}_{N_q} has at least $\Omega(2^{2^{N_q}-N_q-1})$ spanning trees [34]. The tree structure follows Pascal's triangle using a breadth-first search (BFS) approach for computational efficiency. This structure ensures the tree depth is bounded by $L = N_q$. We collect the sign determination results of N_{tree} randomly generated spanning trees, then employ a majority voting scheme with a vote threshold of 50%. The full HRF algorithm is included in the section S.1. The pre-processing step is independent of the quantum state structure, including rank and sparsity, and only depends on the system size N_q . The tree generation time has an exponential cost as the minimal operation on a graph is $\Omega(V)$, where V is the number of nodes. While generating the tree has an exponential cost, it is a one-time computation. Once constructed, the tree can be cached and reused for any N_q qubit configuration.

2.2 Sampling cost and error analysis

Next, we analyze the error bounds of using different sample sizes $N_{\text{samp.}}$ and random trees N_{tree} . First, we estimate the probability of a single sign error between ψ_j and ψ_{j+2^k} is $\Pr(\tilde{s}_{j,j+2^k} \neq s_{j,j+2^k}) \leq \exp(-2N_{\text{samp.}}|\psi_j|^2|\psi_{j+2^k}|^2)$ according to the Hoeffding's inequality [35], where \tilde{s} is the estimated sign using HRF. Figure 3 (a) shows that the larger the product $\psi_j\psi_{j+2^k}$, the easier it becomes to resolve their relative sign with fewer shots. Then, one can analyze the error propagation on each tree. Since every sign at node j is determined by a unique path of edges from the root ψ_0 of length $d_j \leq L$, the estimated \tilde{s}_j is the product of the estimated relative signs along this path. If any edge on the path has an inference error, then the estimated sign flips parity for an odd number of errors. Assuming (for simplicity) that each edge has the same error probability $p_e := \Pr(\tilde{s}_{j,j+2^k} \neq s_{j,j+2^k})$ and errors are independent, the probability p_j that \tilde{s}_j is incorrect can be calculated as

$$p_j \leq \frac{1 - (1 - 2p_e)^L}{2}. \quad (5)$$

In the regime $p_eL \ll 1$, one recovers $p_j \approx p_eL$. But a moderate $p_e = 0.01$ can lead to unreliable predictions deeper in the tree at 10 qubits as $p_j \approx 0.1$. The effective error rate becomes exponentially smaller by combining N_{tree} random trees. Assuming that each tree has an independent error rate $p_j < 1/2$, the probability of returning the wrong signs after majority voting is

$$\Pr_{\text{HRF}}(\tilde{s}_j \neq s_j) \leq \exp(-2N_{\text{tree}}(1/2 - p_j)^2). \quad (6)$$

If each independent tree has an error rate $p_j = 0.1$, then $N_{\text{tree}} = 11$ trees suffice for a sign error below 3%, as shown in fig. 3 (b). If one allows the error budget to be a small fraction of the nodes δ have sign errors, we require $N_{\text{samp.}} \geq \ln(L/\delta)/(2m^2)$ to maintain $p_j < 1/2$ and $N_{\text{tree}} \geq \ln(1/\delta)/(2(1/2 - p_j)^2)$, where $m = \min_{j,k} |\psi_j\psi_{j+2^k}|$ is the minimal overlap.

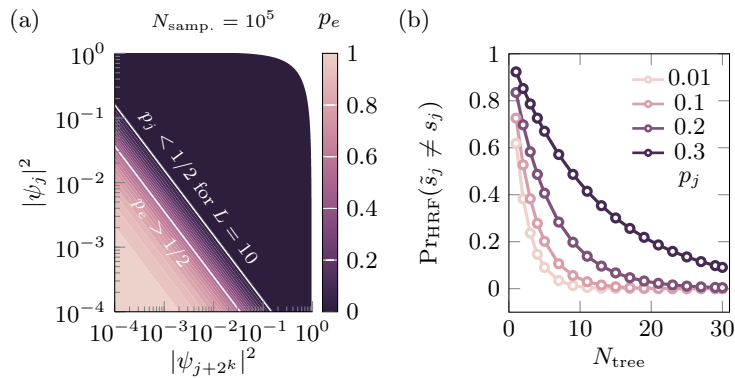


FIG. 3: (a) Probability p_e of returning a sign error between node j and $j + 2^k$ using 10^5 samples, where the variables are constrained with $|\psi_j|^2 + |\psi_{j+2^k}|^2 \leq 1$. For 10-qubit states ($L = 10$), it requires $p_e < 0.05$ such that $p_j < 1/2$ and each tree behaves better than a random guess. (b) Probability of estimating the sign s_j wrong after majority voting with different p_j and N_{tree} .

3 Results

3.1 Benchmarks on IBM quantum hardware

We demonstrate the HRF method and compare its performance and runtime scaling with standard FQST in the Pauli basis on `ibm_fez`, the latest IBM Heron r2 superconducting quantum processor. Figure 4 (e) shows the readout and native two-qubit gate (CZ) error rates. We select a 10-qubit chain from the device to ensure a lower readout error, which is the dominant error source. The real-valued quantum states were generated using the hardware-efficient ansatz [36], but the gate set is limited to $R_y(\theta_j)$ rotation gates on each qubit and $\text{CNOT}_{j,j+1}$ on adjacent qubits. To minimize the influence of two-qubit gate errors, we use a constant shallow depth state preparation circuit $U_{\text{prep.}}$ that consists of 4 layers of R_y gates and $4(N_q - 1)$ pair-wise CNOT gates inside. We use measurement error mitigation for the FQST and HRF experiments by inversion of an assignment matrix [37]. We adopt the X_+X_- dynamical decoupling sequence [38–40] to suppress decoherence during qubit idling time.

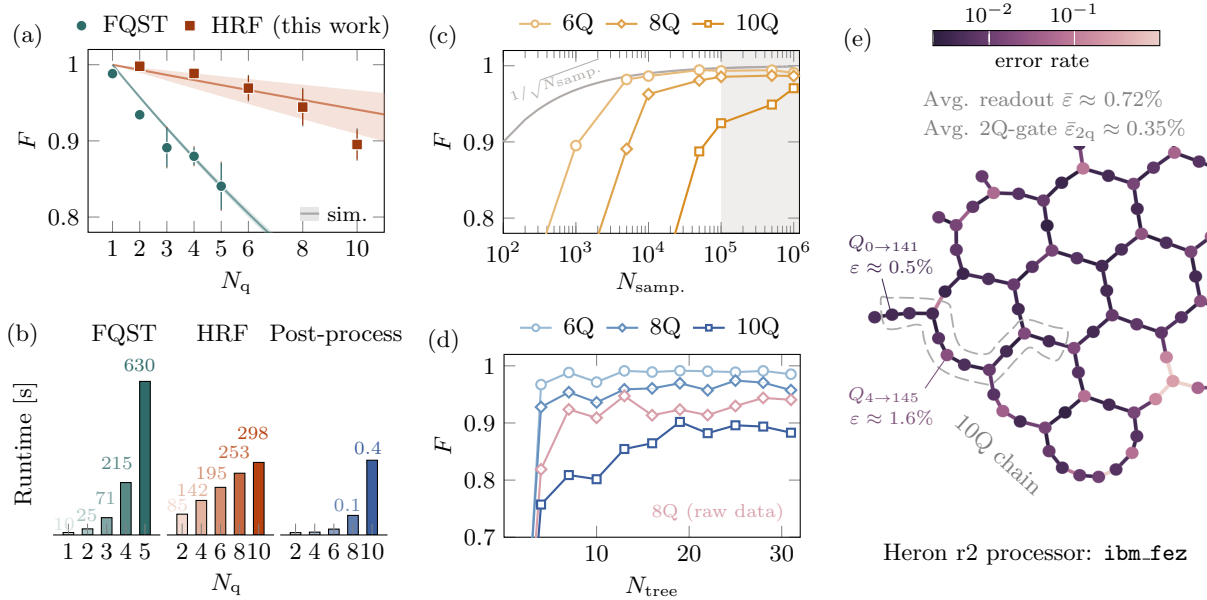


FIG. 4: (a) The fidelities of the reconstructed state with those obtained from FQST and HRF method running on `ibm_fez` quantum processor. (b) Runtime (seconds) scaling of FQST, HRF on `ibm_fez` and post-processing time using 111 trees. (c) The impact of samples $N_{\text{samp.}}$ to fidelities on noisy simulator. The solid gray line represents the upper bound limited by finite sampling noise $\epsilon \approx 1/\sqrt{N_{\text{samp.}}}$ and $N_{\text{samp.}} = 10^5$ is the maximal sample size used in experiments. (d) The impact of the number of trees N_{tree} used in post-processing for sign determination based on samples with and without error mitigation. (e) Readout error ϵ and 2 qubit gate error $\bar{\epsilon}_{2q}$, and single-qubit error $\epsilon_{1q} \sim 10^{-4}$.

For FQST cases, we reconstruct the density matrix ρ up to 5 qubits by measuring 3^{N_q} global observables with $N_{\text{samp.}} = 10^4$ samples for each observable. The 5 qubit FQST experiment takes about 10 min to measure $3^5 = 243$ observables on `ibm_fez`. In contrast, HRF requires only 18 s of sampling time for the same problem size. The experiments were performed sequentially without interruption from periodic calibrations. Thus, the total running time, including error mitigation

overhead, accurately reflects the circuit execution time, providing a faithful measure of the protocol’s efficiency and the experimental resources required.

Performing FQST for up to 10 qubits can be time-consuming (~ 6 h) on actual hardware. For HRF, we reconstruct the state vector $|\psi\rangle$ up to 10 qubits by sampling $N_q + 1 = 11$ circuits with $N_{\text{samp.}} = 10^5$ samples for $N_q > 5$ and $N_{\text{samp.}} = 10^4$ samples for $N_q \leq 5$ to ensure fair fidelity comparison with FQST. The transpiled 10 qubit circuit is $2.54\mu\text{s}$ long and the average T_2 coherence time on the 10 qubit chain of `ibm_fez` is $135.74\mu\text{s}$. We provide more detailed hardware calibration in the supplementary information. Noisy simulations conducted in this study use the same calibration data.

First, we confirm the feasibility of HRF in real-valued state reconstruction and demonstrate its superiority over FQST in terms of accuracy and runtime scaling. [Figure 4](#) (a) shows the fidelity $F(\rho, \tilde{\rho}) = \text{Tr} [\sqrt{\sqrt{\rho}\tilde{\rho}\sqrt{\rho}}]^2$ between the exact state ρ and reconstructed state from hardware $\tilde{\rho}$, where $\tilde{\rho} = |\tilde{\psi}\rangle\langle\tilde{\psi}|$ for HRF. The average fidelity among $R = 5$ random states reaches 84.05% for 5 qubit FQST and 89.53% for 10 qubit HRF after 2.43×10^6 and 1.10×10^6 total samples, respectively. These experimental results are consistent with the noisy simulations shown in the shaded region using $R = 10$ random states. HRF exhibits a higher average fidelity with fewer samples, but larger variance due to randomness in post-processing. So, the reconstructed state has a smaller statistical bias with respect to the true fidelity of 1, but may exhibit higher variance due to fewer measurements (shots). This bias–variance trade-off is common in quantum state tomography on noisy devices [24]. In practice, the community often prioritizes reducing bias over variance, as bias represents a systematic error, whereas variance can be suppressed by averaging over more samples [41].

[Figure 4](#) (b) presents the linear runtime scaling for sample collection using $N_{\text{samp.}} = 10^5$ and a $\Omega(2^{N_q})$ scaling in post-processing, where the latter part can leverage parallel computing to distribute the workload on multiple CPUs since \mathcal{Q}_{N_q} is always bipartite [34]. The largest FQST reconstruction takes 3.35 h post-processing time for a 14-qubit state [42] while HRF would take only 22 s post-processing time for the same problem size using $N_{\text{tree}} = 300$.

We show the impact of sample size $N_{\text{samp.}}$ and the number of trees N_{tree} in [fig. 4](#) (c) and (d) via simulations. The 10 qubit HRF fidelity could reach 97.05% using $N_{\text{samp.}} = 10^6$ samples on a noisy simulator. As the state size increases, more samples are required to reach the finite sampling limit, as indicated by the solid gray curve. We observe that as more samples are collected, the estimated fidelity converges rapidly and asymptotically approaches the limit set by the sampling noise. This suggests that fluctuations in protocol performance are primarily due to statistical noise, with no additional sources of error, indicating the protocol’s efficiency and stability. For post-processing, the reconstructed state fidelity converges after doing majority voting using $N_{\text{tree}} \approx 30$ spanning trees on the corresponding hypercube graph. As illustrated in the pink curve (raw samples without error mitigation), higher-fidelity sampling data with measurement error mitigation would impact the final reconstructed state fidelity $\sim 3\%$. The overhead introduced is a few extra hardware calibrations, which require approximately 10 s for 10 qubit states.

3.2 Quantum state property and overlap estimation

In this section, we apply the HRF method to evaluate nonlinear state properties including the logarithmic negativity $E_N(\rho)$ for entanglement quantification [43], α -stabilizer Rényi entropy $M_\alpha(|\psi\rangle)$ for quantifying quantum magic [44], and overlap $S_\ell(|\psi\rangle)$ between a classical index state $|\psi_\ell\rangle$ that resembles a numerical integration along the path ℓ . [Figure 5](#) (a) compares the logarithmic negativity

$$E_N(\tilde{\rho}) = \log_2 \|\tilde{\rho}^{\Gamma_A}\|_1 \quad (7)$$

calculated from HRF (on `ibm_fez`) and exact values, where ρ^{Γ_A} is the partial transpose with respect to $\lceil N_q/2 \rceil$ qubits subsystem A and $\|\cdot\|_1$ denotes the trace norm. The relative difference r is defined as $|E_N(\rho) - E_N(\tilde{\rho})|/|E_N(\rho)|$. The predicted value from the HRF method agrees well with the exact numerical value, except for the 10 qubit case. On the other side, magic states are the resource that allows quantum computers to attain an advantage over classical computers. One common magic measure is the α -stabilizer Rényi entropy [44], defined as

$$M_\alpha(|\psi\rangle) = \frac{1}{1-\alpha} \log_2 \left(\sum_{\sigma \in \mathcal{P}} 2^{-N_q} \langle \psi | \sigma | \psi \rangle^{2\alpha} \right), \quad (8)$$

where α is the entropic index and \mathcal{P} is the set of 4^{N_q} Pauli strings. Given its importance, we measure the 2-stabilizer entropy $M_2(|\tilde{\psi}\rangle)$ of 3 random real-valued states on `ibm_fez`, as shown in [fig. 5](#) (b). The results closely match an exact evaluation.

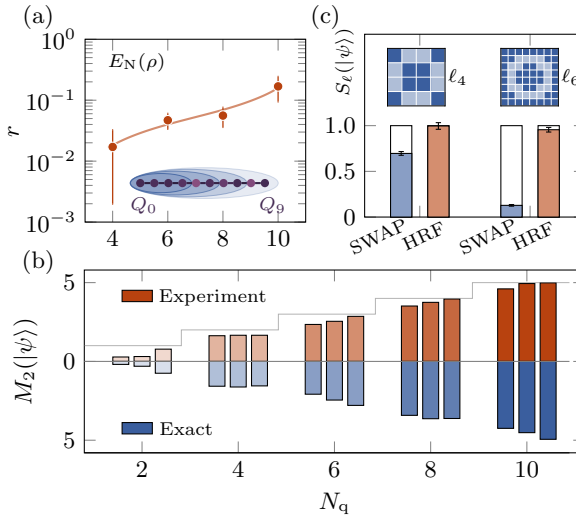


FIG. 5: Estimating quantum state properties using the reconstructed state $|\tilde{\psi}\rangle$ from HRF. (a) Log-negativity of $N_q \in \{4, 6, 8, 10\}$ on the 10-qubit chain of `ibm_fez`. (b) Stabilizer entropy of $R = 3$ random states on `ibm_fez`. (c) State overlap (noisy simulation) that resembles a numerical integration over a circle in the domain, where ℓ_4 and ℓ_6 are integration paths for 4- and 6-qubit.

We use HRF to estimate the overlap $S_\ell(|\psi\rangle) = |\langle \psi_{\ell_{N_q}} | \psi \rangle|^2$ where $\{\ell_{N_q}\}$ is a circle path in a 2D lattice of size $[2^{N_q/2}, 2^{N_q/2}]$ as illustrated in [fig. 5](#) (c), and $|\psi_{\ell_{N_q}}\rangle = \frac{1}{N} \sum_{j \in \{\ell_{N_q}\}} |j\rangle$ is the corresponding

state by concatenating the lattice row-wise for a normalization constant \mathcal{N} . This quantity resembles a numerical integration over the path ℓ_{N_q} , which can occur, for example, when calculating drag and lift coefficients for computational fluid mechanics simulations [14], scattering cross sections in electromagnetism simulations [45], among others. Through noisy simulations, we compare the estimated overlap with the standard SWAP test [46]. The SWAP test requires $2N_q + 1$ qubits in total, and the explicit circuit construction with estimated hardware execution time is shown in [fig. S2](#). The accuracy of the SWAP test decreases with increasing problem size N_q due to hardware noise, whereas HRF maintains a high fidelity of $\geq 95\%$ (averaged over $R = 5$ random states).

3.3 Quantum linear system solve

In this section, we firstly use the variational quantum linear solver (VQLS) [33] shown in [fig. 6](#) (a) to solve a linear system $\mathbf{A} |x\rangle = |b\rangle$ inspired by the Ising model under noiseless simulation. Then, we apply the HRF method to readout the solution state and benchmark its performance on `ibm_fez`. The Ising-inspired quantum linear system problem [33] can be written as

$$\mathbf{A} = \frac{1}{\zeta} \left(\sum_{k=0}^{N_q-1} \sigma_x^k + J \sum_{k=0}^{N_q-2} \sigma_z^k \sigma_z^{k+1} + \eta \mathbb{I} \right) \quad \text{and} \quad |b\rangle = \bigotimes_{k=0}^{N_q-1} R_y(\theta^k) |0\rangle^{\otimes N_q}, \quad (9)$$

where J is the coupling strength, ζ and η are normalization factors to control the matrix condition number $\kappa(\mathbf{A}) := \|\mathbf{A}\| \|\mathbf{A}^{-1}\|$ such that the smallest eigenvalue of \mathbf{A} is $1/\kappa$ and largest eigenvalue of 1. Under this evaluation, we set $J = 0.1$ and $\kappa = 2$. The sparsity pattern of matrix \mathbf{A} is illustrated in [fig. 6](#) (b). The state preparation circuit V for the right-hand side vector $|b\rangle$ consists of one layer of R_y rotation on each qubit, and the rotation angles θ^k are chosen randomly from $[-\pi, \pi]$ applied on the k -th qubit.

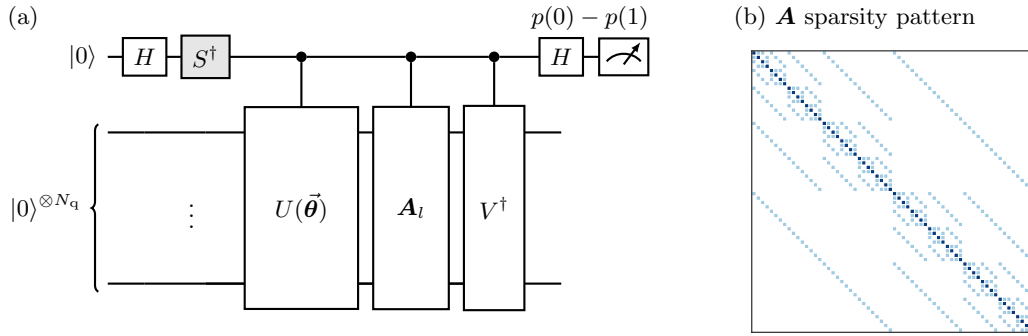


FIG. 6: (a) VQLS circuit for evaluating the cost function $C(\vec{\theta})$ with the Hadamard test, which uses one ancilla qubit initialized in $|0\rangle$ and a controlled unitary sandwiched with two Hadamard gates. Then, one can calculate $\text{Re}\langle 0|V^\dagger \mathbf{A}_l U(\vec{\theta})|0\rangle = p(0) - p(1)$, where $p(0)$ and $p(1)$ are the probabilities of measuring 0 and 1 in the ancilla qubit. (b) Visualization of the matrix structure of $\mathbf{A}_{64 \times 64}$ in a 6-qubit Ising-inspired linear system problem.

The VQLS algorithm essentially uses the Hadamard test [47] to estimate the cost function $C(\vec{\theta}) = 1 - |\langle b|\Psi\rangle|^2$, where $|\Psi\rangle = \mathbf{A}|\psi\rangle / \sqrt{\langle \psi|\mathbf{A}^\dagger \mathbf{A}|\psi\rangle}$ and $|\psi\rangle = U(\vec{\theta})|0\rangle^{\otimes N_q}$ is the quantum iterative solution prepared using the same hardware-efficient ansatz as in [section 3.3.1](#). Hence, the cost function has

an operational meaning similar to the absolute residual $\| |b\rangle - \mathbf{A}|\psi\rangle \|$. Then, one can optimize over the parameters $\vec{\theta} = (\theta_1, \dots, \theta_m)$ to minimize the cost function and obtain an approximate solution $|\psi^*\rangle$. It is usually assumed that matrix \mathbf{A} is decomposed into a linear combination of unitaries (LCU) $\mathbf{A} = \sum_{l=1}^{L_a} c_l \mathbf{A}_l$. For the Ising-inspired linear system problem in (9), each \mathbf{A}_l is a Pauli operator and c_l is a real number.

After solving the linear system, we apply the HRF method to readout the solution state $|\psi^*\rangle$ for $N_q \in \{3, 4, 5, 6, 7\}$ qubits with the noiseless simulation, noisy simulation based on hardware noise modeling, and actual quantum hardware `ibm_fez`. The results measuring the fidelity between the VQLS solution $|\psi^*\rangle$ and the reconstructed state by the HRF method $|\tilde{\psi}\rangle$ are shown in fig. 7. The hardware results are consistent with noisy simulation behavior, and one can observe the performance improvement from error mitigation. HRF reconstructs the 7 qubit solution state with high fidelity $F = 91.55\%$ by using 8×10^5 total samples.

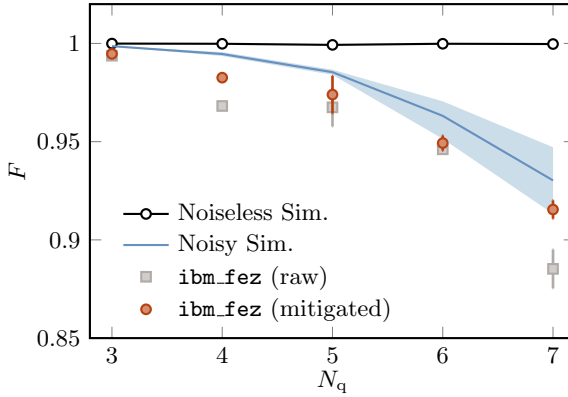


FIG. 7: Reconstructing the solution state from a variational quantum linear solver.

4 Conclusion

We present an asymptotically faster technique for reconstructing real-valued quantum states. HRF reduces the exponential measurement settings in FQST from an exponential number to a linear one. Still, the post-processing time remains exponential, though it can be mitigated via parallel computing on classical devices. We experimentally demonstrate our approach on an IBM superconducting quantum processor. Using the superposition of amplitudes and a random forest algorithm as a post-processing tool, we reconstruct the random 10 qubit real-valued states with high fidelity $F \approx 89\%$ and a 7 qubit solution state from the Ising-inspired quantum linear system problem with fidelity $F \approx 92\%$. HRF accurately estimates state properties such as quantum entanglement, magic, and state overlap estimation from near-term hardware sampling results. This improvement paves the way for end-to-end applications based on QLSA and many application problems on near-term and early fault-tolerant devices. The method may also shed light on other strictly real-valued quantum tomography techniques, such as process tomography.

Data availability

The code and data used for this manuscript is permissively (MIT) licensed and available at <https://github.com/comp-physics/Quantum-HRF-Tomography>.

Competing interests

The authors declare no competing interests.

Acknowledgments

We acknowledge the use of IBM Quantum services for this work. The views expressed are those of the authors and do not reflect the official policy or position of IBM or the IBM Quantum team. This research used resources of the Oak Ridge Leadership Computing Facility, which is a DOE Office of Science User Facility supported under Contract DE-AC05-00OR22725.

- [1] J. Liu, M. Liu, J.-P. Liu, Z. Ye, Y. Wang, Y. Alexeev, J. Eisert, L. Jiang, Towards provably efficient quantum algorithms for large-scale machine-learning models, *Nature Communications* **15** (2024) 434.
- [2] X. Li, X. Yin, N. Wiebe, J. Chun, G. K. Schenter, M. S. Cheung, J. Mülmenstädt, Potential quantum advantage for simulation of fluid dynamics, *Physical Review Research* **7** (2025) 013036.
- [3] M. R. Hestenes, E. Stiefel, Methods of conjugate gradients for solving linear systems, *Journal of Research of the National Bureau of Standards* **49** (1952).
- [4] Y. Saad, M. H. Schultz, Gmres: A generalized minimal residual algorithm for solving nonsymmetric linear systems, *SIAM Journal on Scientific and Statistical Computing* **7** (1986) 856–869.
- [5] A. M. Childs, R. Kothari, R. D. Somma, Quantum algorithm for systems of linear equations with exponentially improved dependence on precision, *SIAM Journal on Computing* **46** (2017) 1920–1950.
- [6] P. C. Costa, D. An, Y. R. Sanders, Y. Su, R. Babbush, D. W. Berry, Optimal scaling quantum linear-systems solver via discrete adiabatic theorem, *PRX Quantum* **3** (2022) 040303.
- [7] G. H. Low, Y. Su, Quantum linear system algorithm with optimal queries to initial state preparation, arXiv preprint arXiv:2410.18178 (2024).
- [8] M. E. Morales, L. Pira, P. Schleich, K. Koor, P. Costa, D. An, A. Aspuru-Guzik, L. Lin, P. Rebentrost, D. W. Berry, Quantum linear system solvers: A survey of algorithms and applications, arXiv preprint arXiv:2411.02522 (2024).
- [9] S. Aaronson, Read the fine print, *Nature Physics* **11** (2015) 291–293.
- [10] H.-Y. Huang, R. Kueng, J. Preskill, Predicting many properties of a quantum system from very few measurements, *Nature Physics* **16** (2020) 1050–1057.
- [11] H.-Y. Huang, Learning quantum states from their classical shadows, *Nature Reviews Physics* **4** (2022) 81–81.
- [12] D. Grinko, J. Gacon, C. Zoufal, S. Woerner, Iterative quantum amplitude estimation, *npj Quantum Information* **7** (2021) 52.
- [13] A. Manzano, D. Musso, Á. Leitao, Real quantum amplitude estimation, *EPJ Quantum Technology* **10** (2023) 1–24.

- [14] J. Penuel, A. Katabarwa, P. D. Johnson, C. Farquhar, Y. Cao, M. C. Garrett, Feasibility of accelerating incompressible computational fluid dynamics simulations with fault-tolerant quantum computers, arXiv preprint arXiv:2406.06323 (2024).
- [15] A. Patterson, L. Lapworth, Measurement schemes for quantum linear equation solvers, *Quantum Science and Technology* **10** (2025) 025037.
- [16] R. Blume-Kohout, T. Proctor, K. Young, Quantum characterization, verification, and validation, arXiv preprint arXiv:2503.16383 (2025).
- [17] H. Ren, Y. Li, Modeling quantum devices and the reconstruction of physics in practical systems, *Physical Review Letters* **123** (2019) 140405.
- [18] R. Shaffer, H. Ren, E. Dyrenkova, C. G. Yale, D. S. Lobser, A. D. Burch, M. N. Chow, M. C. Revelle, S. M. Clark, H. Häffner, Sample-efficient verification of continuously-parameterized quantum gates for small quantum processors, *Quantum* **7** (2023) 997.
- [19] U. Leonhardt, Quantum-state tomography and discrete wigner function, *Physical Review Letters* **74** (1995) 4101.
- [20] Z. Hradil, Quantum-state estimation, *Physical Review A* **55** (1997) R1561.
- [21] D. Gross, Y.-K. Liu, S. T. Flammia, S. Becker, J. Eisert, Quantum state tomography via compressed sensing, *Physical Review Letters* **105** (2010) 150401.
- [22] M. Cramer, M. B. Plenio, S. T. Flammia, R. Somma, D. Gross, S. D. Bartlett, O. Landon-Cardinal, D. Poulin, Y.-K. Liu, Efficient quantum state tomography, *Nature Communications* **1** (2010) 149.
- [23] J. Cotler, F. Wilczek, Quantum overlapping tomography, *Physical Review Letters* **124** (2020) 100401.
- [24] Z. Yang, S. Ru, L. Cao, N. Zheludev, W. Gao, Experimental demonstration of quantum overlapping tomography, *Physical Review Letters* **130** (2023) 050804.
- [25] M. K. Kurmapu, V. Tiunova, E. Tiunov, M. Ringbauer, C. Maier, R. Blatt, T. Monz, A. K. Fedorov, A. Lvovsky, Reconstructing complex states of a 20-qubit quantum simulator, *PRX Quantum* **4** (2023) 040345.
- [26] Y. Guo, S. Yang, Quantum state tomography with locally purified density operators and local measurements, *Communications Physics* **7** (2024) 322.
- [27] C.-K. Hu, C. Wei, C. Liu, L. Che, Y. Zhou, G. Xie, H. Qin, G. Hu, H. Yuan, R. Zhou, et al., Experimental sample-efficient quantum state tomography via parallel measurements, *Physical Review Letters* **133** (2024) 160801.
- [28] L. K. Grover, A fast quantum mechanical algorithm for database search, in: *Proceedings of the Twenty-Eighth Annual ACM Symposium on the Theory of Computing*, 1996, pp. 212–219.
- [29] E. Bernstein, U. Vazirani, Quantum complexity theory, in: *Proceedings of the twenty-fifth annual ACM symposium on Theory of computing*, 1993, pp. 11–20.
- [30] N. Delfosse, P. Allard Guerin, J. Bian, R. Raussendorf, Wigner function negativity and contextuality in quantum computation on rebits, *Physical Review X* **5** (2015) 021003.
- [31] M. West, A. A. Mele, M. Larocca, M. Cerezo, Real classical shadows, arXiv preprint arXiv:2410.23481 (2024).
- [32] T. K. Ho, Random decision forests, in: *Proceedings of 3rd international conference on document analysis and recognition*, volume 1, IEEE, 1995, pp. 278–282.
- [33] C. Bravo-Prieto, R. LaRose, M. Cerezo, Y. Subasi, L. Cincio, P. J. Coles, Variational quantum linear solver, *Quantum* **7** (2023) 1188.
- [34] F. Harary, J. P. Hayes, H.-J. Wu, A survey of the theory of hypercube graphs, *Computers & Mathematics with Applications* **15** (1988) 277–289.
- [35] W. Hoeffding, Probability inequalities for sums of bounded random variables, *Journal of the American statistical association* **58** (1963) 13–30.
- [36] A. Kandala, A. Mezzacapo, K. Temme, M. Takita, M. Brink, J. M. Chow, J. M. Gambetta, Hardware-efficient variational quantum eigensolver for small molecules and quantum magnets, *Nature* **549** (2017) 242–246.

- [37] P. D. Nation, H. Kang, N. Sundaresan, J. M. Gambetta, Scalable mitigation of measurement errors on quantum computers, *PRX Quantum* **2** (2021) 040326.
- [38] V. Tripathi, H. Chen, M. Khezri, K.-W. Yip, E. Levenson-Falk, D. A. Lidar, Suppression of crosstalk in superconducting qubits using dynamical decoupling, *Physical Review Applied* **18** (2022) 024068.
- [39] S. Niu, A. Todri-Sanial, Effects of dynamical decoupling and pulse-level optimizations on ibm quantum computers, *IEEE Transactions on Quantum Engineering* **3** (2022) 1–10.
- [40] N. Ezzell, B. Pokharel, L. Tewala, G. Quiroz, D. A. Lidar, Dynamical decoupling for superconducting qubits: A performance survey, *Physical Review Applied* **20** (2023) 064027.
- [41] C. Schwemmer, L. Knips, D. Richart, H. Weinfurter, T. Moroder, M. Kleinmann, O. Gühne, Systematic errors in current quantum state tomography tools, *Physical Review Letters* **114** (2015) 080403.
- [42] Z. Hou, H.-S. Zhong, Y. Tian, D. Dong, B. Qi, L. Li, Y. Wang, F. Nori, G.-Y. Xiang, C.-F. Li, et al., Full reconstruction of a 14-qubit state within four hours, *New Journal of Physics* **18** (2016) 083036.
- [43] M. B. Plenio, Logarithmic negativity: a full entanglement monotone that is not convex, *Physical Review Letters* **95** (2005) 090503.
- [44] L. Leone, S. F. Oliviero, A. Hamma, Stabilizer rényi entropy, *Physical Review Letters* **128** (2022) 050402.
- [45] B. D. Clader, B. C. Jacobs, C. R. Sprouse, Preconditioned quantum linear system algorithm, *Physical Review Letters* **110** (2013) 250504.
- [46] H. Buhrman, R. Cleve, J. Watrous, R. De Wolf, Quantum fingerprinting, *Physical Review Letters* **87** (2001) 167902.
- [47] D. Aharonov, V. Jones, Z. Landau, A polynomial quantum algorithm for approximating the jones polynomial, in: Proceedings of the thirty-eighth annual ACM symposium on Theory of computing, 2006, pp. 427–436.
- [48] V. Havlíček, A. D. Córcoles, K. Temme, A. W. Harrow, A. Kandala, J. M. Chow, J. M. Gambetta, Supervised learning with quantum-enhanced feature spaces, *Nature* **567** (2019) 209–212.
- [49] Y. Liu, S. Arunachalam, K. Temme, A rigorous and robust quantum speed-up in supervised machine learning, *Nature Physics* **17** (2021) 1013–1017.
- [50] A. Elben, B. Vermersch, R. Van Bijnen, C. Kokail, T. Brydges, C. Maier, M. K. Joshi, R. Blatt, C. F. Roos, P. Zoller, Cross-platform verification of intermediate scale quantum devices, *Physical Review Letters* **124** (2020) 010504.
- [51] F. Mintert, M. Kuš, A. Buchleitner, Concurrence of mixed multipartite quantum states, *Physical Review Letters* **95** (2005) 260502.
- [52] A. K. Ekert, C. M. Alves, D. K. Oi, M. Horodecki, P. Horodecki, L. C. Kwek, Direct estimations of linear and nonlinear functionals of a quantum state, *Physical Review Letters* **88** (2002) 217901.

Supplemental Material

S.1 SUPPLEMENTARY NOTE 1: Details of HRF

S.1.1 Algorithm description via pseudocode

Algorithm 1 Hadamard Random Forest (HRF)

Require: Number of qubits N_q , sample size for each circuit $N_{\text{samp.}}$, number of trees N_{tree}

Ensure: Reconstruct real state vector $|\psi\rangle \in \mathbb{R}^{2^{N_q}}$

```

1: Prepare  $N_{\text{samp.}}$  copies of  $|\psi\rangle$  using  $U_{\text{prep.}}$ 
2: Measure all  $N_q$  qubits in  $\sigma_z$  basis
3: for all  $j \in \{0, \dots, 2^{N_q} - 1\}$  do
4:    $|\tilde{\psi}_j|^2 \leftarrow$  empirical frequency in basis  $|j\rangle$ 
5: end for
6: for  $k = 0$  to  $N_q - 1$  do
7:   Prepare  $N_{\text{samp.}}$  copies of  $|\psi\rangle$  using  $U_{\text{prep.}}$ 
8:   Measure the  $(N_q - k - 1)$ -th qubit in  $\sigma_x$  basis
9:   Measure the rest qubits in  $\sigma_z$  basis
10:  for all  $j \in \{0, \dots, 2^{N_q} - 1\}$  do
11:     $|\tilde{\psi}_j^k|^2 \leftarrow$  empirical frequency in basis  $|j\rangle$ 
12:  end for
13: end for                                     ▷ 1. Collect samples

14: for  $i = 1$  to  $N_{\text{tree}}$  do           ▷ 2. Build random forest
15:    $T_i \leftarrow$  a random spanning tree on  $\mathcal{Q}_{N_q}$  using BFS
16:   Initialize root sign  $s_0^{(i)} \leftarrow +1$ 
17:   for all unique path from node 0  $\rightarrow j$  in  $T_i$  do
18:     for all valid  $(n, k)$  along path do
19:       Compute relative signs
20:        $s_{n,n+2^k}^{(i)} \leftarrow \text{sgn}(2|\tilde{\psi}_n^k|^2 - |\tilde{\psi}_n|^2 - |\tilde{\psi}_{n+2^k}|^2)$ 
21:        $s_j^{(i)} \leftarrow s_{j,j-2^k}^{(i)} \times \dots \times s_{2^k,0}^{(i)} \times s_0^{(i)}$ 
22:     end for
23:   end for
24: end for                                     ▷ 3. Majority voting

25: for all  $j \in \{0, \dots, 2^{N_q} - 1\}$  do
26:    $s_j \leftarrow \text{sgn}\left(\sum_{i=1}^{N_{\text{tree}}} s_j^{(i)}\right)$ 
27: end for                                     ▷ 4. Reconstruct state

28: for all  $j \in \{0, \dots, 2^{N_q} - 1\}$  do
29:    $|\tilde{\psi}_j| \leftarrow \sqrt{|\tilde{\psi}_j|^2}$ 
30:    $\tilde{\psi}_j \leftarrow s_j \times |\tilde{\psi}_j|$ 
31: end for
32: return  $|\tilde{\psi}\rangle$ 

```

S.1.2 Quantum circuit construction

We use the hardware-efficient ansatz to prepare real-valued states as shown in [fig. S1](#). The parameters are chosen uniformly from the interval $[-\pi/2, \pi/2]$.

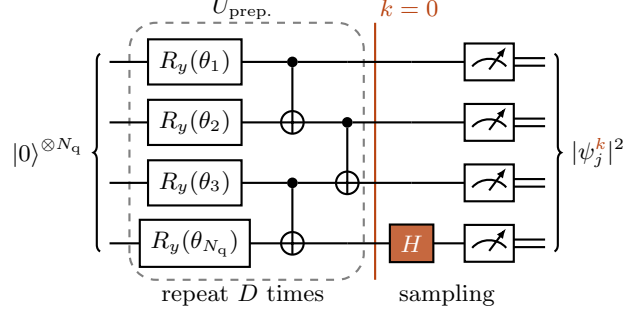


FIG. S1: State preparation and measurement circuits for HRF. The largest case on the IBM hardware benchmark [section 3.3.1](#) contains 36 CZ gates.

S.1.3 Hardware calibration data

[Table S1](#) shows the hardware calibration data used throughout the manuscript.

Qubit	T_1 (μs)	T_2 (μs)	Meas. error ε	2Q gate error ε_{2q}
Q_0	184	101	4.64×10^{-3}	2.74×10^{-3}
Q_1	188	237	4.88×10^{-3}	2.69×10^{-3}
Q_2	216	173	4.39×10^{-3}	3.02×10^{-3}
Q_3	171	248	6.34×10^{-3}	3.35×10^{-3}
Q_4	142	111	1.56×10^{-2}	3.35×10^{-3}
Q_5	197	31	5.62×10^{-3}	3.48×10^{-3}
Q_6	170	152	9.28×10^{-3}	5.54×10^{-3}
Q_7	140	138	4.15×10^{-3}	3.42×10^{-3}
Q_8	154	111	1.29×10^{-2}	3.65×10^{-3}
Q_9	98	57	4.64×10^{-3}	/
Avg.	166	136	7.24×10^{-3}	3.47×10^{-3}

TABLE S1: Device properties of `ibm_fez` at the time each experiment reported in this paper was performed. The readout length is $t_{\text{mea.}} = 1560$ ns and native 2Q gate (CZ) with pulse length $t_{2q} = 84$ ns for all qubits.

S.2 SUPPLEMENTARY NOTE 2: MEASUREMENT SCHEMES

S.2.1 Quantum Amplitude Estimation

Compared to quantum amplitude estimation (QAE) [12, 13], HRF employs shallow circuits with easily implementable gates. QAE is optimal for estimating a specific amplitude or a few dominant

amplitudes. Still, it requires deep, coherent circuits with controlled unitaries, which are challenging to implement and prone to errors. HRF offers a more scalable alternative that recovers all the amplitudes simultaneously instead of running QAE sequentially, making HRF well-suited for near-term quantum applications. **table S2** provides a detailed comparison of HRF and QAE.

Feature	QAE	HRF (this work)
Objective	Estimate single amplitude of general complex quantum states	Reconstruct full state vector of real-valued quantum states
Circuit Depth	Deep (uses Grover-like subroutines)	Shallow (single-layer Hadamards)
Measurements	Controlled unitaries with ancilla	σ_z, σ_x only
Qubit Overhead	$N_q + 1$ or more (ancilla + control)	N_q
Sample Complexity	Optimal $\mathcal{O}(1/\epsilon)$	Trade more samples for shallow circuits
NISQ Suitability	Low; Error-prone	High; Error-robust

TABLE S2: Comparison between Quantum Amplitude Estimation and Hadamard Random Forest.

S.2.2 Quantum state overlap estimation

Here, we show a concrete example of how HRF can simplify the task of estimating the overlap $S = |\langle \psi | \phi \rangle|^2$ between two unknown quantum states $|\psi\rangle$ and $|\phi\rangle$. Such a task has applications in quantum machine learning [48, 49] and cross-platform verification [50]. A widely adopted approach to this problem is the SWAP test [46], which involves applying a controlled-SWAP operation and measuring an ancillary qubit (see **fig. S2**). However, the SWAP test requires direct preparation and entanglement between the two states, making its implementation resource-intensive on near-term devices.

The HRF offers an alternative method for estimating state overlap. Instead of requiring entanglement between $|\psi\rangle$ and $|\phi\rangle$, HRF reconstructs each state independently and computes their overlap classically via post-processing of reconstructed amplitudes. This approach significantly reduces the circuit size by half. It also eliminates the need for controlled-SWAP operations, making it more scalable and implementable for near-term quantum hardware. In larger circuits, like the SWAP test, noise accumulates. Since HRF uses smaller circuits, it is more resilient to noise and can integrate well-established error mitigation methods such as SPAM error cancellation, as demonstrated in this work. The lower circuit complexity also opens up the possibility of further noise reduction techniques.

Regarding sample complexity and scalability, suppose there are R states. The swap test requires circuits involving all R^2 pairs of states, whereas HRF only needs to characterize each of the R states individually, leading to a quadratic speedup in terms of the number of states. We note, however, that HRF shifts the expensive cross-state quantum operations into classical post-processing, with a trade-off of potentially more measurement shots. Thus, HRF is more advantageous for near-term devices where minimizing quantum circuit depth is crucial. Beyond state overlap estimation, the advantage brought by HRF can also generalize to other tasks involving multi-state property estimation, such as entanglement estimation [51, 52].

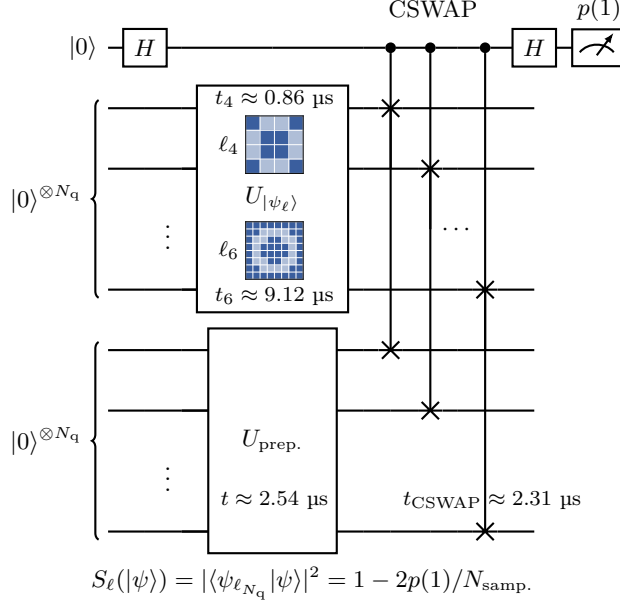


FIG. S2: SWAP test for estimating overlap $S_\ell(|\psi\rangle)$ with transpiled execution time on `ibm_fez` for each block.

In this study, we apply the SWAP test to estimate overlap that resembles a numerical integration over the path ℓ_{N_q} . More specifically, the index state that encodes the 4-qubit path ℓ_4 is shown below

$$\begin{aligned}
 |\psi_{\ell_4}\rangle = & \frac{1}{2\sqrt{2}} (|0001\rangle + |0010\rangle + |0100\rangle + |0111\rangle \\
 & + |1000\rangle + |1011\rangle + |1101\rangle + |1110\rangle). \tag{S1}
 \end{aligned}$$

This happens to be a stabilizer state with $M_2(|\psi_{\ell_4}\rangle) = 0$ but more generally $|\psi_{\ell_6}\rangle$ is not.